



Maps of Solar Wind Plasma Precipitation onto Mercury's Surface: A Geographical Perspective

Federico Lavorenti^{1,2} , Elizabeth A. Jensen³ , Sae Aizawa^{2,4}, Francesco Califano² , Mario D'Amore⁵, Deborah Domingue³ , Pierre Henri^{1,6}, Simon Lindsay⁷ , Jim M. Raines⁸, and Daniel Wolf Savin⁹ 

¹ Laboratoire Lagrange, Observatoire de la Côte d'Azur, Université Côte d'Azur, CNRS, Nice, France

² Dipartimento di Fisica "E. Fermi", Università di Pisa, Pisa, Italy

³ Planetary Science Institute, Tucson, AZ, USA

⁴ Japan Aerospace Exploration Agency, Sagamihara, Kanagawa, Japan

⁵ Institut für Planetenforschung, Deutsches Zentrum für Luft- und Raumfahrt (DLR), Rutherfordstr. 2, D-12489 Berlin, Germany

⁶ LPC2E, CNRS, Univ. d'Orléans, CNES, Orléans, France

⁷ School of Physics and Astronomy, The University of Leicester, Leicester, UK

⁸ Department of Climate and Space Sciences and Engineering, University of Michigan, Ann Arbor, Michigan USA

⁹ Columbia Astrophysics Laboratory, Columbia University, MC 5247, 550 West 120th Street, New York, NY 10027, USA

Received 2023 May 16; revised 2023 August 9; accepted 2023 August 9; published 2023 September 12

Abstract

Mercury is the closest planet to the Sun, possesses a weak intrinsic magnetic field, and has only a very tenuous atmosphere (exosphere). These three conditions result in a direct coupling between the plasma emitted from the Sun (namely, the solar wind) and Mercury's surface. The planet's magnetic field leads to a nontrivial pattern of plasma precipitation onto the surface that is expected to contribute to the alteration of the regolith over geological timescales. The goal of this work is to study the solar wind plasma precipitation onto the surface of Mercury from a geographical perspective, as opposed to the local time-of-day approach of previous precipitation modeling studies. We employ solar wind precipitation maps for protons and electrons from two fully kinetic numerical simulations of Mercury's plasma environment. These maps are then integrated over two full Mercury orbits (176 Earth days). We found that the plasma precipitation pattern at the surface is most strongly affected by the upstream solar wind conditions, particularly the interplanetary magnetic field direction, and less by Mercury's 3:2 spin-orbit resonance. We also found that Mercury's magnetic field is able to shield the surface from roughly 90% of the incoming solar wind flux. At the surface, protons have a broad energy distribution from below 500 eV to more than 1.5 keV, while electrons are mostly found in the range 0.1–10 keV. These results will help to better constrain space weathering and exosphere source processes at Mercury, as well as interpret observations by the ongoing ESA/JAXA BepiColombo mission.

Unified Astronomy Thesaurus concepts: Mercury (planet) (1024); Space weather (2037); Space plasmas (1544); Regolith (2294); Planetary science (1255); Planetary surfaces (2113); Solar wind (1534); Planetary geology (2288); Interplanetary magnetic fields (824); Magnetic fields (994)

1. Introduction

Mercury is the only telluric solar system planet other than Earth with an intrinsic magnetic field (Ogilvie et al. 1974). Mercury's magnetic field shapes the interaction between the planet's surface and the surrounding solar wind, a turbulent, supersonic, and magnetized plasma flowing outward from the Sun (Meyer-Vernet 2007). The interaction between Mercury's magnetic field and the solar wind is a crucial part of the global Hermean environment, both in shape and evolution. This is a result of the planet's proximity to the Sun (0.31 au at perihelion and 0.47 au at aphelion) and its relatively weak magnetic field (around 200 nT at the surface; Anderson et al. 2012).

The interaction between the solar wind and Mercury's magnetic field determines the precipitation of solar wind protons and electrons onto the planet's surface through a complex series of coupled local processes (Slavin 2004; Slavin et al. 2007). On the dayside, the presence of a bow shock in front of the planet along with magnetic reconnection in the magnetopause determines the pattern and energy of the

precipitating plasma, while on the nightside, the precipitating plasma is mostly affected by magnetic reconnection and the magnetic field configuration in the tail. On the dayside, downstream of the bow shock (in the so-called magnetosheath), the plasma density, temperature, and magnetic field increase, while the plasma bulk velocity decreases. This slowdown leads to an order-of-magnitude reduction in the proton kinetic energy, which still dominates over the thermal energy component in the total energy of the protons. This differs with respect to the slowdown in the electron velocity, which does not significantly alter the electron total energy, as the thermal energy component dominates over the kinetic component in the total energy of the electrons. This proton and electron energy partition has been observed in situ at Earth's bow shock (Schwartz et al. 2022) and at interplanetary shocks (David et al. 2022); nonetheless, such in situ observations at Mercury are still lacking. Downstream of the magnetosheath, at the magnetopause, a part of the magnetic field carried by the solar wind connects with Mercury's magnetic field through magnetic reconnection (Dibraccio et al. 2013; Gershman et al. 2013). This process allows a fraction of shocked solar wind plasma to precipitate onto the surface, spiraling along newly opened magnetic field lines (Raines et al. 2022, and references therein). On the nightside, particles are accelerated and ejected



Original content from this work may be used under the terms of the [Creative Commons Attribution 4.0 licence](https://creativecommons.org/licenses/by/4.0/). Any further distribution of this work must maintain attribution to the author(s) and the title of the work, journal citation and DOI.

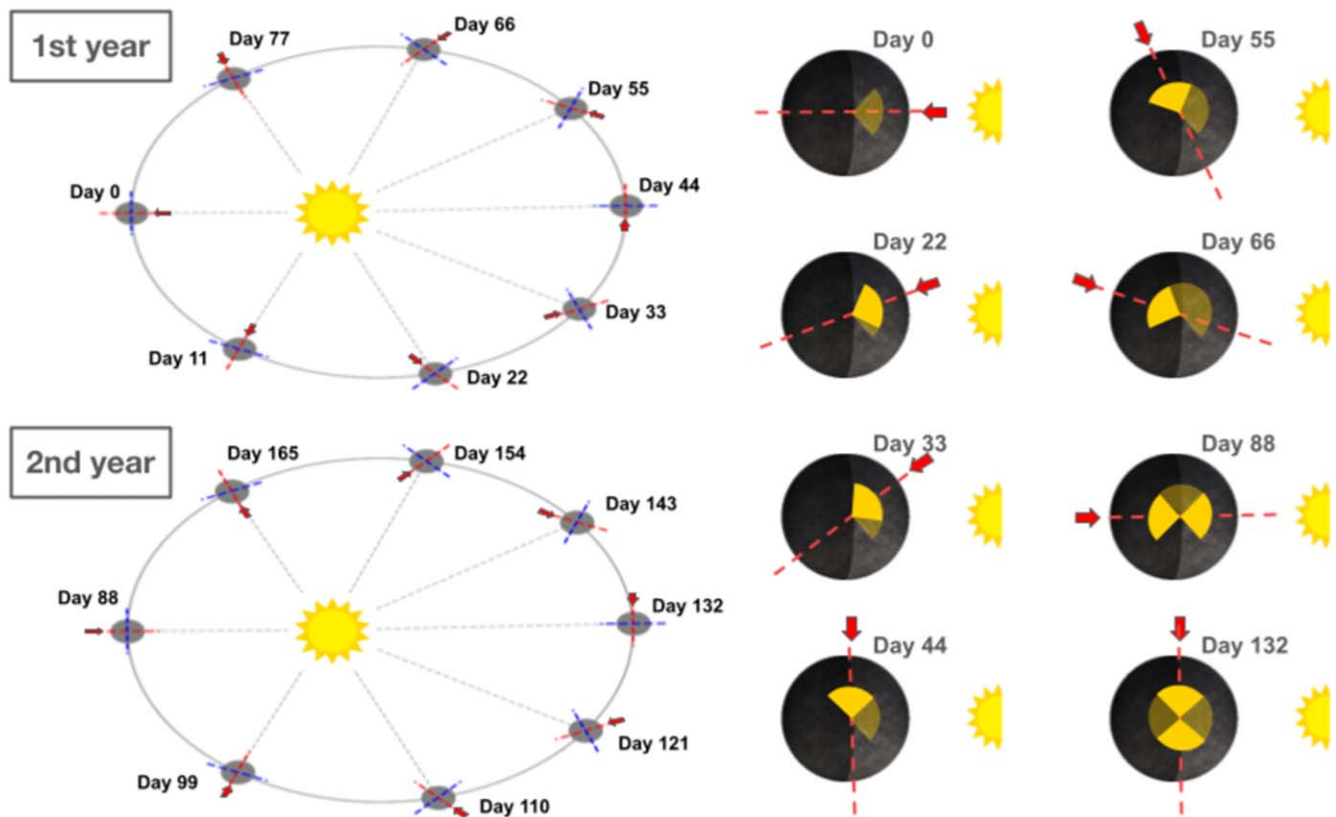


Figure 1. Sketch of plasma precipitation onto Mercury’s surface over orbital time. The 3:2 spin–orbit resonance is responsible for increasing the cusp precipitation at the hot poles (red dashed lines) compared to the warm poles (blue dashed lines). The yellow sectors in the right panel approximately indicate the accumulation of plasma at the cusp over time.

planetward as magnetic field lines reconnect in the tail of the magnetosphere (Poh et al. 2017; Sun et al. 2017; Dewey et al. 2020). This high-energy plasma is accelerated through the plasma sheet horns (i.e., regions connecting the plasma sheet to the surface at midlatitudes, analogous to auroral ovals at Earth) and precipitates onto the surface, spiraling along magnetic field lines (Glass et al. 2022). The magnetic topology of the planet plus solar wind determines, to a large extent, the geographical distribution of plasma precipitation on both sides of the planet.

Plasma precipitation onto the surface of Mercury is further affected by the 3:2 spin–orbit resonance of the planet, as shown in Figure 1. As a consequence of this resonance, an observer standing at longitude 0° (or 180°) faces the Sun for a longer time and at a closer distance compared to longitude 90° (or -90°). Therefore, Mercury’s surface at longitudes 0° and 180° (called the hot poles) experiences a higher mean photon flux than at longitudes 90° and -90° (called the warm poles). This was confirmed by the NASA MESSENGER mission (Solomon et al. 2007), which found a bimodal longitudinal pattern characterized by hot (warm) poles with maximal temperatures of 700 K (570 K; Bauch et al. 2021). A similar longitudinal pattern is expected to arise in the plasma fluxes at the surface when integrating over two full Mercury orbits. Past numerical works have addressed this problem in terms of “time of day” (local time) on the surface (Massetti et al. 2003, 2007; Mura et al. 2005; Kidder et al. 2008; Benna et al. 2010; Schriver et al. 2011; Fatemi et al. 2020; Lavorenti et al. 2023), but plasma precipitation has yet to be examined with regard to geographic location.

Looking at plasma precipitation from a geographic perspective will enable a correlation of plasma fluxes with spectral and compositional properties of the surface and thus an exploration of potential causal relationships with space weathering driven by the solar wind. Precipitation of solar wind particles onto the surface of Mercury drives space-weathering processes such as ion sputtering, ion implantation, electron-stimulated desorption (ESD), and X-ray fluorescence (XRF; Domingue et al. 2014; Wurz et al. 2022). Ion irradiation affects the surface at an atomic level and the exosphere at a global level. Ion sputtering is thought to be one of the main source processes for high-altitude sodium in the Hermean exosphere (Mangano et al. 2015; Exner et al. 2020; Killen et al. 2022). The maps presented in this work will allow researchers to better quantify ion sputtering at the surface of Mercury by relating the geographical distributions of ion fluxes with the surface distribution of sputtered species. ESD is another poorly understood source process of Mercury’s exosphere (Madelé et al. 1998; McLain et al. 2011; Domingue et al. 2014). The electron maps computed in this work, coupled with maps of surface temperature and composition, will enable a precise description of ESD for exosphere models. Driven by \sim keV electrons, XRF converts precipitating electrons to X-ray photons at the surface of Mercury (Lindsay et al. 2016, 2022; Lavorenti et al. 2023). Future X-ray observations at Mercury by the joint ESA/JAXA BepiColombo mission (Benkhoff et al. 2021) will benefit from the electron precipitation maps computed in this work. The BepiColombo/MIXS instrument (Bunce et al. 2020) will be able to constrain the surface

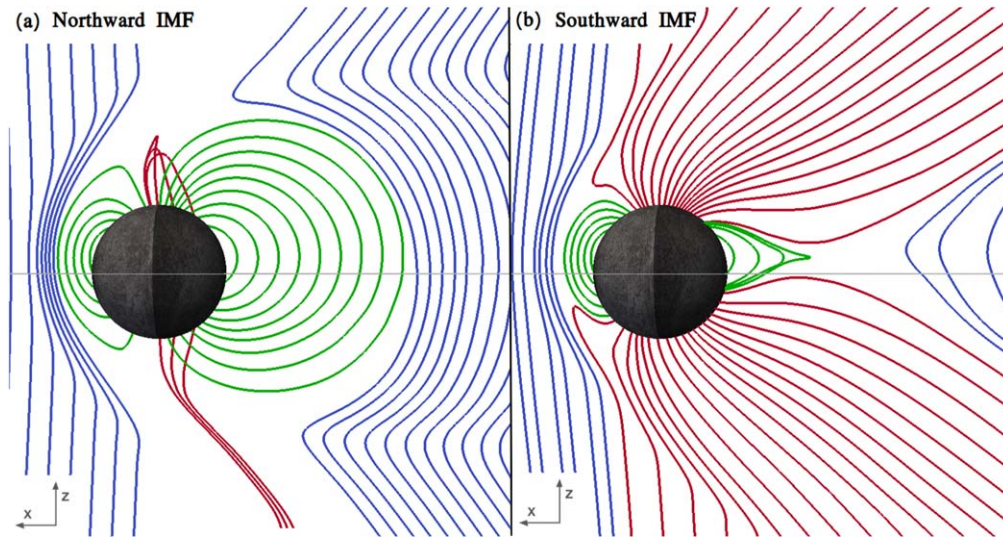


Figure 2. Magnetic field lines in the meridian plane (the X - Z plane in the Mercury-centered solar orbital coordinate system) for our two simulations. The left (right) panel corresponds to a simulation with a northward (southward) IMF. Blue lines correspond to magnetic field lines not connected to the planet (i.e., solar wind field lines). Red lines correspond to magnetic field lines with one end connected to the planet (i.e., magnetospheric open field lines). Green lines correspond to magnetic field lines with both ends connected to the planet (i.e., magnetospheric closed field lines). The horizontal gray lines indicate the geographic equator of the planet.

composition and mineralogy in part by using solar wind electrons to “probe” the Hermean surface via XRF.

Here we present the first plasma precipitation maps at Mercury integrated over two full Mercury orbits (176 Earth days) to account for the spin-orbit resonance. We use the proton and electron precipitation maps published in Lavorenti et al. (2023) as a function of “time of day” as inputs to our computations over Mercury’s orbit. In this work, we neglect heavy solar wind ions (with atomic number $Z \geq 2$), micro-meteoroid impacts, and thermal processes acting at the surface. The rest of the paper is organized as follows. Section 2 describes the methods used in this work. Section 3 presents the results with a focus on the spatial and energy distribution of particles at the surface of Mercury. In Section 4, we discuss the implications of our results for Mercury science and, more broadly, for space weathering of weakly magnetized bodies. Section 5 summarizes the conclusions of the paper.

2. Methods

We utilize the proton and electron precipitation maps published in Lavorenti et al. (2023), which were computed using a fully kinetic, global, three-dimensional plasma model of Mercury’s magnetosphere. This numerical model solves the Vlasov–Maxwell system of equations using an implicit particle-in-cell (PIC) algorithm (Markidis et al. 2010). The model solves the plasma dynamics of the interaction between the solar wind and Mercury’s magnetic field, self-consistently including the kinetic physics of both protons and electrons. Kinetic models differ from other fluid plasma models (e.g., magnetohydrodynamic models) that do not take into account the velocity distribution functions of the particles but use only averaged quantities such as density, bulk velocity, pressure, etc. In our simulations, the normalized planetary radius, the proton-to-electron mass ratio, and the light-to-Alfvén speed ratio are artificially reduced in order to be able to run on state-of-the-art high-performance computing facilities while maintaining a good—although compressed—separation of scales between the planetary radius, proton gyroradius, and electron gyroradius. This approach was validated in Lavorenti et al. (2022) by

comparing the bow shock and magnetopause positions from our model with the ones observed in situ by MESSENGER and averaged over the mission time period (Winslow et al. 2013). The artificially reduced scales used in our model induce a nonnegligible increase of proton nonadiabatic effects, as compared to the real system. This effect is important, for instance, in the ion diffusion region in the tail (extending ~ 10 ion skin depths from the reconnection line) that reaches the planet surface in our simulations. However, rescaling techniques analogous to the ones used in this work were used in past hybrid models for Mercury (Trávníček et al. 2007, 2009, 2010; Schriver et al. 2011) and global models of Earth’s magnetosphere (Tóth et al. 2017) to compensate for the lack of sufficient computational resources. A detailed discussion of this rescaling technique can be found in Lavorenti et al. (2023, Appendix A).

The solution of our numerical model depends upon the upstream solar wind parameters. We use solar wind parameters corresponding to typical mean values at Mercury’s aphelion (Sarantos et al. 2007; James et al. 2017) with plasma density $n_{sw} = 30 \text{ cm}^{-3}$, speed $V_{sw} = 400 \text{ km s}^{-1}$, magnetic field amplitude $B_{sw} = 20 \text{ nT}$, and proton and electron temperatures $T_{i,sw} = T_{e,sw} = 21.5 \text{ eV}$. These parameters are kept fixed in our two numerical simulations, while we vary the direction of the interplanetary magnetic field (IMF) in our two runs from purely northward to purely southward. Different directions of the IMF correspond to different magnetic configurations at the surface of Mercury, as shown in Figure 2. These configurations, in turn, affect plasma precipitation at the surface. In this work, we address two extreme IMF configurations (with $B_x = B_y = 0$) rarely found in the real system, but which are useful to grasp the role of the magnetic field in shaping the plasma precipitation at the surface. Our IMF configurations show the range of variability of the system by providing conditions for minimal (maximal) magnetic coupling between the solar wind and the planet when the IMF is northward (southward), i.e., when the IMF is antiparallel (parallel) to the planetary magnetic dipole moment.

Plasma precipitation maps as a function of local time were integrated along two full Mercury orbits, from 2022 January 23

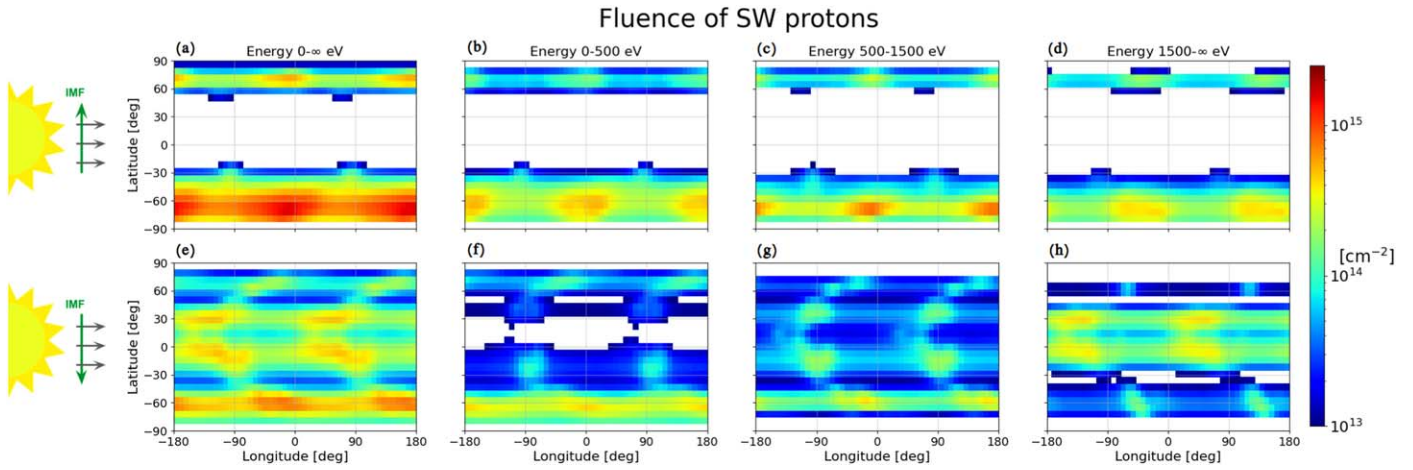


Figure 3. Proton precipitation maps integrated over two full Mercury orbits. Panels (a)–(d) are obtained from a simulation with a purely northward IMF and panels (e)–(h) with a purely southward IMF, shown by the green vectors on the left. The different columns correspond to different energy bins, given at the top of each column. At perihelion, when longitude 0° is subsolar, longitudes -90° and $+90^\circ$ correspond to local dawn and dusk, respectively. The white bins in the maps correspond to negligible fluences below 10^{13} cm^{-2} .

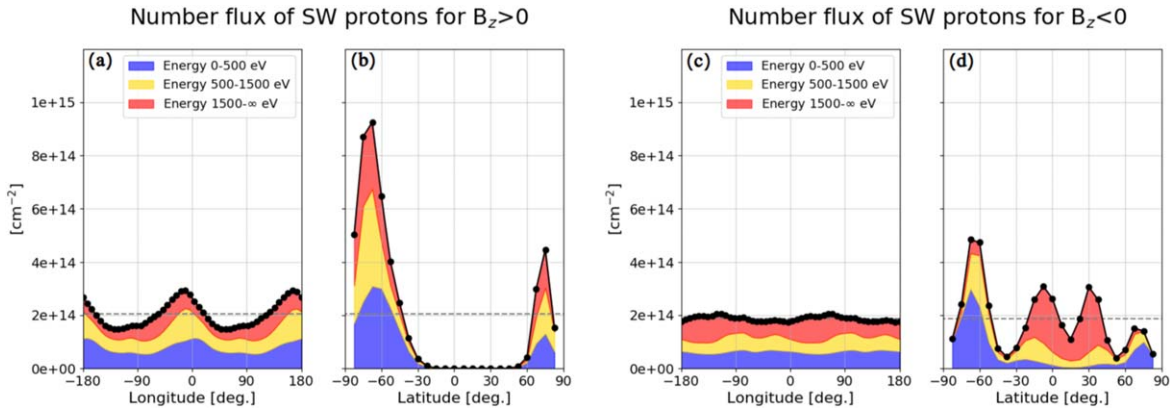


Figure 4. Proton precipitation maps integrated over two full Mercury orbits and averaged over latitude and longitude. The curves in panels (a) and (c) are obtained from the maps in Figures 3(a)–(d) and (e)–(h), respectively, by averaging in latitude. The curves in panels (b) and (d) are obtained, respectively, from the same maps by averaging in longitude. The black dots and line show the averages summed over all energies, and the colored areas show the contributions for the labeled energy bins. The horizontal dashed black lines show the mean value of the fluence (averaged in both latitude and longitude).

at 18:44:32 UTC to 2022 July 18 at 05:48:44 UTC; this corresponds to the time interval shown in Figure 1. We do not consider variations in the solar wind parameters along the orbit, which will be included in a future work that also includes a more realistic IMF configuration. We subdivide the orbit into 515 steps of equal time $dt = 8.21$ hr. At each time step, we rotate the planet and map the local time to surface longitude using the Jet Propulsion Laboratory’s Navigation and Ancillary Information Facility (NAIF) SPICE files and routines. The NAIF/SPICE files enable a precise determination of the location of the Sun with respect to Mercury at each time of the orbit and consist of ephemeris files for the orbit of Mercury and planetary body information for its rotation. The geographical registration of local time to longitude through this time period is provided with the ancillary files to this publication (Lavorenti et al. 2023).

3. Results

3.1. Spatial Distribution of Particle Fluxes at the Surface

The spatial distribution of particle fluxes at the surface is organized into latitudinal bands with enhancements in longitude driven by the 3:2 resonance. For protons, this pattern is

shown by the maps in Figure 3, along with the latitudinal and longitudinal averages in Figure 4. The proton data are shown for energy bins of 0–500, 500–1500, and 1500– ∞ eV, which we refer to as low, moderate, and high energies. For electrons, Figures 5 and 6 show the corresponding data. The electron data are shown for energy bins of 0–100, 100–1000, and 1000– ∞ eV, which we refer to as low, moderate, and high energies. The results from these maps are summarized in Table 1 using a coarse spatial grid and averaging between the two IMF conditions under study. In these maps, longitudinal variations are controlled by Mercury’s rotation, while latitudinal variations are controlled by the IMF. In the following, we discuss these two effects separately.

Mercury’s rotation is responsible for the differential accumulation of particles versus longitude. Due to the 3:2 spin–orbit resonance of Mercury, subsolar (local time 12 hr) high-latitude proton precipitation is enhanced at the hot poles (longitude 0° and 180°), as shown in Figure 3. This effect is more prominent in the simulation with a northward IMF, as shown in Figures 3(a)–(d) and 4(a). Under a northward IMF, the topology of the magnetosphere (i.e., the “closed” topology shown in Figure 2(a)) channels plasma precipitation to the high-latitude cusps at local time 12 hr. This hot pole

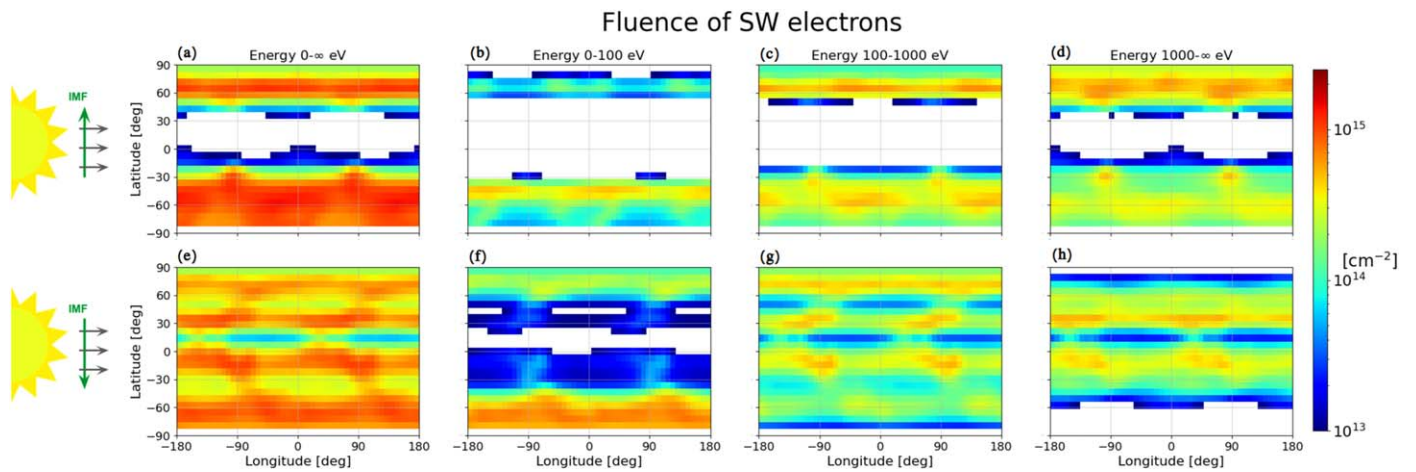


Figure 5. Same as Figure 3, but for electron precipitation.

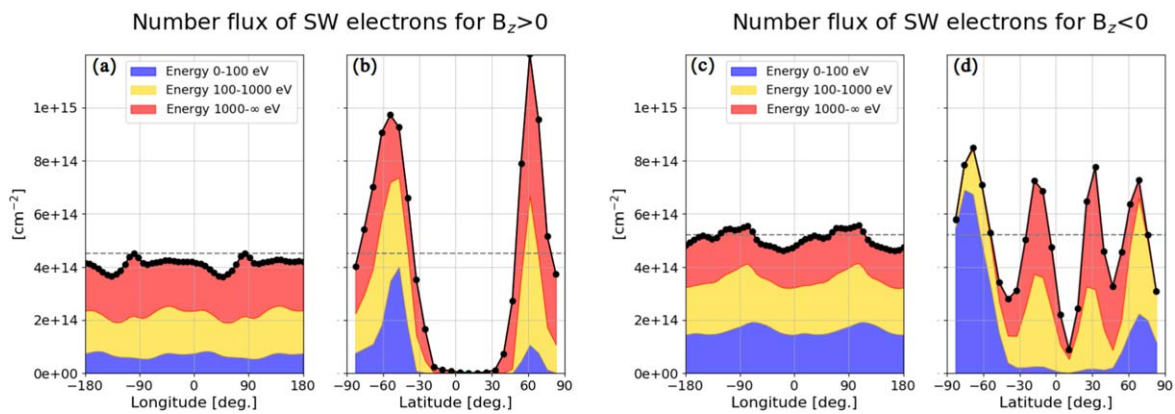


Figure 6. Same as Figure 4, but for electron precipitation.

enhancement shifts downward (by roughly -20° longitude, as shown in Figure 4(a)) with increasing proton energy. This energy-dependent shift is consistent with a grad-B drift of protons when approaching Mercury’s surface and its higher magnetic field, as shown by Mura et al. (2005) using a test particle model. Under a southward IMF and the resulting “open” magnetic field topology of the magnetosphere shown in Figure 2(b), plasma precipitation occurs both at the cusps and at low latitudes. Cusp precipitation is enhanced at the hot poles due to the same mechanism at play with the northward IMF, as shown in Figures 3(e)–(g). This contrasts with the low-latitude proton precipitation, as shown in Figures 3(g) and (h). These low-latitude protons are ejected from the reconnection site in the tail and precipitate between roughly midnight and dawn in local time (Lavorenti et al. 2022, 2023). This is due to the combined action of the \mathbf{ExB} (grad-B) drift that pushes protons downward (duskward) in the magnetotail that results, in the end, in a proton enhancement at dawn. This is in agreement with MESSENGER observations showing a more prominent proton population at dawn, as compared to dusk (Korth et al. 2011). Proton precipitation around dawn in local time translates to precipitation around the warm poles in geographical coordinates.

Electrons precipitate onto the surface of Mercury with a pattern somewhat similar to that of the protons, as both are driven by the magnetic field topology. Longitudinal enhancements for electrons are weaker than for protons due to their

higher thermal energy component (that accounts for random motion) as compared to their kinetic energy component (that accounts for ordered motion). This means that, although electrons are more magnetized, they have a higher random velocity parallel to the magnetic field, as compared to protons, and this drives a “background” precipitation of thermal electrons from the solar wind directly onto the surface along open magnetic field lines. Under a northward IMF, electron precipitation in the cusps is enhanced around the hot poles at high latitude, as shown in Figures 5(a)–(c). In this case, the “closed” magnetosphere topology channels electrons at high latitudes and inhibits electron precipitation at low latitudes. Under a southward IMF, the electron precipitation presents two distinct regions of precipitation, the high-latitude low-energy electrons in Figure 5(f) and the low-latitude moderate- and high-energy electrons in Figures 5(g) and (h). Both tend to be enhanced around the warm poles, as shown in Figure 6(c), although these enhancements are quite weak. These enhancements at the warm poles are a direct consequence of electron precipitation toward dawn in local time (Lindsay et al. 2022; Lavorenti et al. 2023).

Variations in the IMF drive strongly different latitudinal particle distributions at the surface. Under a northward IMF, Mercury’s magnetic dipole is able to shield a large fraction of the planet from the impinging solar wind. In this case, protons and electrons precipitate mostly onto the cusps at high latitudes. Protons precipitate between latitudes 70° – 80° N and

Table 1
Particle Fluences in Units of 10^{14} cm^{-2} for Different Regions at the Surface of Mercury, Averaged over the Two IMF Simulations

	Energy [eV]	North Pole	Equatorial Region	South Pole
Proton fluence [10^{14} cm^{-2}]	0–500	0.9	Small	1.8
	500–1500	0.8	Small	1.2
	1500– ∞	0.5	0.7	0.9
Electron fluence [10^{14} cm^{-2}]	0–100	1.8	Small	2.8
	100–1000	3.0	2.0	2.0
	1000– ∞	4.1	2.5	2.4

Note. North pole corresponds to latitudes from $+90^\circ$ to $+60^\circ$. Equatorial region corresponds to latitudes from $+60^\circ$ to -30° . South pole corresponds to latitudes below -30° . The entries “small” in the table indicate negligible fluence values that are below $0.5 \times 10^{14} \text{ cm}^{-2}$.

-45°S to -90°S , as shown in Figure 4(b). Electrons precipitate between latitudes $60^\circ\text{--}80^\circ\text{N}$ and -30°S to -70°S , as shown in Figure 6(b). The north–south asymmetry in the size of the cusp precipitation region is a consequence of the northward shift of Mercury’s magnetic dipole. The position of the northern cusp is in agreement with recent estimates by Raines et al. (2022) using MESSENGER/FIPS data. Under a northward IMF, particle precipitation is negligible in the equatorial region at latitudes spanning from $+60^\circ$ to -30° . Conversely, under a southward IMF, the topology of the magnetosphere results in stronger precipitation at low latitudes, as shown in Figures 4(d) for protons and 6(d) for electrons. This low-latitude precipitating plasma is composed of high-energy protons and moderate- and high-energy electrons ejected planetward from the reconnection site in the tail. Respectively, comparing Figures 4(b) and (d) with Figures 4(a) and (c) for protons or, equivalently, Figures 6(b) and (d) with Figures 6(a) and (c) for electrons, we observe that latitudinal variations driven by the IMF are about 1 order of magnitude more important than longitudinal variations driven by Mercury’s rotation.

The dependence of proton precipitation on the IMF was investigated by Massetti et al. (2003, 2007), Mura et al. (2005), and Sarantos et al. (2007) using test-particles models and by Kallio & Janhunen (2003) and Fatemi et al. (2020) using global hybrid models. Overall, they found that (i) magnetic reconnection can increase the proton energy up to some keV with fluxes of the order of $10^8\text{--}10^9 \text{ cm}^{-2} \text{ s}^{-1}$, and (ii) the precipitation pattern is strongly dependent on the IMF direction, in particular that a (planetward) sunward component of the IMF increases the proton precipitation onto the (northern) southern hemisphere and that a larger B_z component increases the area of open magnetic field lines—and thus of precipitation—onto the surface. Our results build upon the findings of these past works and extend our current view of plasma precipitation onto the surface of Mercury by (i) including electrons self-consistently in the model and (ii) computing the precipitation in geographical coordinates instead of the commonly used “time-of-day” coordinates.

A coarse energy sampling of the precipitation maps in three energy bins, shown in Figures (3)–(6), enables one to identify the importance of various particle distributions in driving different processes at the surface. The fluences of the particles in each of the three energy bins are summarized in Table 1 using a coarse spatial grid and averaging over the two IMF

configurations under study. In this table, we show the mean fluence of protons and electrons in each energy bin in three regions at the surface of Mercury, namely, the north pole (above 60° latitude), the equatorial region (from 60° to -30° latitude) and the south pole (below -30° latitude). These fluence values can be used for a first-order estimate of space weathering due to plasma–surface interaction processes at Mercury. This point is further discussed in Section 4.

3.2. Energy Distribution of Particles at the Surface

For protons, the net effect of Mercury’s magnetic field is to broaden their energy distribution. In our simulations, solar wind protons are initialized with a narrow Maxwellian energy distribution centered around $m_i V_{\text{sw}}^2/2 = 826 \text{ eV}$, corresponding to a solar wind speed of $V_{\text{sw}} = 400 \text{ km s}^{-1}$ (shown by the red vertical solid lines in Figures 7(a) and (b)). The distribution width is of the order of $T_{i,\text{sw}} = 21.5 \text{ eV}$, as shown by the orange curves in Figure 7(a) and (b). At the surface, the energy distribution of protons spreads out to a few keV, with a considerable population centered around $\sim 200 \text{ eV}$, as shown by the blue curves in Figure 7(a) and (b). Two competing processes are at play to slow down some of the solar wind protons and accelerate others. The slowdown of solar wind protons is due to the presence of a bow shock in front of the planet. Upon passing through the bow shock, protons are decelerated from the (upstream) solar wind speed of $V_{\text{sw}} = 400 \text{ km s}^{-1}$ to the (downstream) fast magnetosonic speed $V_f = (V_{A,i}^2 + V_{s,i}^2)^{1/2}$ (Belmont et al. 2019). The fast magnetosonic speed in the solar wind is $V_f = 120 \text{ km s}^{-1}$, corresponding to a kinetic energy of 76 eV (shown by the green vertical dashed lines in Figures 7(a) and (b)). In principle, V_f should be computed using the density, temperature, and magnetic field values in the magnetosheath, but given the uncertainty associated with these values, here we use as a lower limit the fast magnetosonic speed in the solar wind, where $V_{A,i} = B_{\text{sw}}/\sqrt{4\pi m_i n_{\text{sw}}}$ is the Alfvén speed, $V_{s,i} = \sqrt{\gamma T_{i,\text{sw}}/m_i}$ is the ion sound speed, and $\gamma = 2$ is the adiabatic index of the plasma. The acceleration of solar wind protons is due to magnetic reconnection in the magnetosphere. For a northward IMF, magnetic reconnection is weakly driven at the lobes at high latitudes. For a southward IMF, magnetic reconnection is more strongly driven both at the nose and in the tail of the magnetosphere. Magnetic reconnection converts part of the magnetic energy stored in the planetary magnetic field configuration, corresponding to roughly 10 keV (shown by the green vertical solid lines in Figures 7(a) and (b)), to the kinetic energy of the particles. The efficiency of this conversion is on the order of 10% (Phan et al. 2014; Shay et al. 2014; Haggerty et al. 2015), meaning that roughly 1 keV of magnetic field energy is converted to the kinetic energy of the particles. These two competing processes (bow shock slowdown and acceleration by magnetic reconnection) are responsible for the proton fluences versus energy at the surface reported in Table 1. Substantial proton fluences below 500 eV —mostly at high latitudes—are a consequence of the plasma slowdown downstream of the bow shock, while proton fluences above 1.5 keV —mostly at high latitudes under a northward IMF or low latitudes under a southward IMF—are a consequence of magnetic reconnection and proton heating in the magnetosheath. This result has implications for current estimates of ion sputtering at Mercury that consider ions with a fixed energy of 1 keV amu^{-1} to approximate the solar wind proton energy

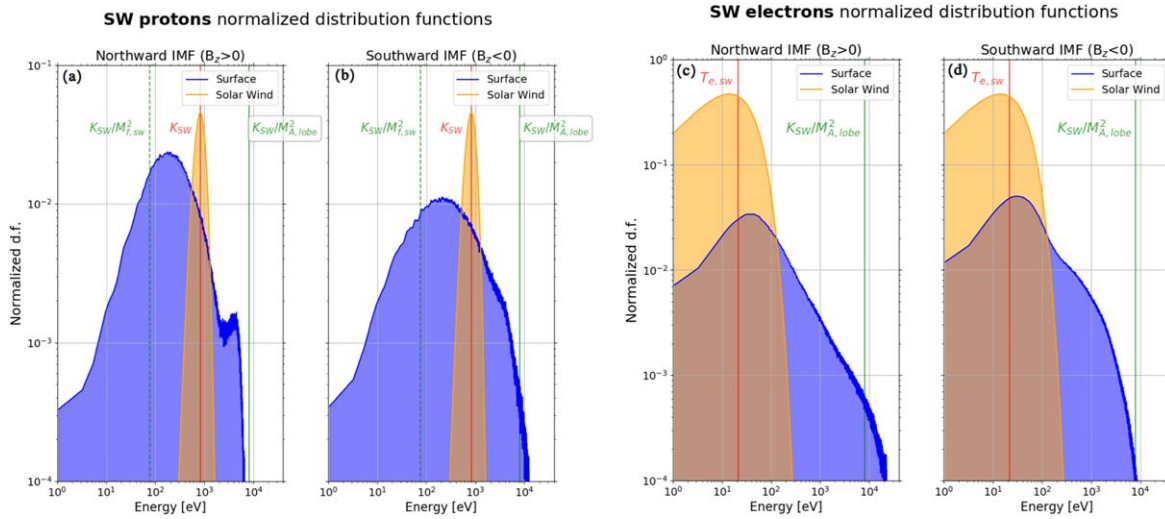


Figure 7. Normalized energy distribution of the particles in the solar wind (orange) and at the surface (blue). Panels (a) and (b) show the proton distribution functions. Panels (c) and (d) show the electron distribution functions. The red vertical solid lines show the mean energy of the solar wind plasma, which is equal to $K_{sw} = m_i V_{sw}^2 / 2 = 826$ eV for protons and $T_{e,sw} = 21.5$ eV for electrons. The green vertical dashed lines in panels (a) and (b) show an estimate of the proton energy downstream of the bow shock equal to $K_{sw}/M_{f,sw}^2$, where $M_{f,sw} = 3.3$ is the fast magnetosonic Mach number in the solar wind upstream of the bow shock. The green vertical solid lines show an estimate of the maximum magnetic energy available for magnetic reconnection equal to $K_{sw}/M_{A,lobe}^2$, where $M_{A,lobe} = 0.32$ is the Alfvén Mach number in the lobes computed using a magnetic field of 100 nT and density of 3 cm^{-3} .

upstream of the bow shock, i.e., Killen et al. (2022) and Morrissey et al. (2022). A broader discussion of the impact of proton energy distributions on sputtering yield can be found in Section 4.2.

For electrons, the net effect of Mercury’s magnetic field is energization by magnetic reconnection. Solar wind electrons have a Maxwellian energy distribution with temperature $T_{e,sw} = 21.5$ eV, as shown by the orange curves in Figure 7(c) and (d). For electrons, the flow energy component $m_e V_{sw}^2 / 2 = 8.26$ eV (in the solar wind) is negligible with respect to the thermal energy component both outside and inside Mercury’s magnetosphere. At the surface, the electron energy distribution displays a high-energy tail extending up to ~ 10 keV, as shown by the blue curves in Figures 7(c) and (d). Magnetic reconnection energizes a substantial fraction of solar wind electrons up to the maximum magnetic energy available, shown by the green vertical solid lines in Figures 7(c) and (d). As a consequence, precipitating electrons are mostly found in the moderate- and high-energy bins with energies above hundreds of eV, as summarized by the fluences in Table 1.

4. Discussion and Implications

The study of solar wind particle precipitation on weakly magnetized bodies (such as Mercury) is more complex than that on unmagnetized bodies (such as the Moon). The presence of an intrinsic magnetic field—although weak—has a considerable effect on both where particles precipitate onto the surface and what energy these particles have. In the following, we discuss these two effects separately and their implications for plasma–surface interaction processes. Particular relevance is given to the comparison between weakly magnetized and unmagnetized bodies.

4.1. Magnetosphere as a Filter: The Effect of a Magnetic Field on the Spatial Distribution of Particles at the Surface

We consider here the interaction between a homogeneous, constant flow of plasma (i.e., an ideal solar wind) and a

spherical body (i.e., an ideal rocky body such as Mercury or the Moon). The body rotates with angular velocity ω and a spin axis perpendicular to the plasma flow. If the body is unmagnetized, the flux of particles reaching the surface integrated over a time $\Delta T \gg 2\pi/\omega$ corresponds to the solar wind fluence multiplied by the cross-sectional area πR^2 and divided by the total surface body area $4\pi R^2$:

$$\frac{n_{sw} V_{sw} \Delta T}{4} \quad (1)$$

If the body is weakly magnetized, the fluence of particles at the surface is further reduced by a factor $\alpha > 1$ as follows:

$$\frac{n_{sw} V_{sw} \Delta T}{4\alpha} \quad (2)$$

The effective shielding parameter α accounts for the average reduction of plasma flux from the solar wind onto the surface due to the magnetic field. From the averaged fluences reported in Figure 4 for protons and Figure 6 for electrons, we derive the effective shielding parameters for solar wind protons and electrons:

$$\alpha_p \approx 20, \quad (3)$$

$$\alpha_e \approx 10. \quad (4)$$

Our results indicate that the magnetic field effectively shields about 90% of the incoming solar wind particles, reducing the fluence at the surface by 1 order of magnitude as compared to the unmagnetized case. Similar shielding values were reported by Massetti et al. (2003) and Mura et al. (2005), focusing on proton precipitation at the cusps. The shielding values do not vary appreciably between our two runs using a purely northward or southward IMF, suggesting that the IMF direction weakly affects the total number of particles precipitating onto the surface. Raines et al. (2022) found a similar weak dependence in their estimates of cusp precipitation (their Figure 8(c)). A future study using a more realistic IMF

direction for Mercury (including B_x and B_y components) will address this point specifically.

The IMF direction controls where solar wind particles precipitate onto the surface. Although the total number of precipitating particles weakly depends on the IMF direction, at least for the configurations under study, the regions of strongest precipitation significantly differ between the simulations with a purely northward and southward IMF, as shown in Section 3.1. Therefore, time variations in the IMF direction—not included in our computation—would modify the location of the regions of strongest particle precipitation. Since the IMF direction changes on timescales of the order of tens of minutes due to the turbulence in the solar wind (James et al. 2017), we expect a continuously changing pattern of precipitation. The natural variability of the solar wind density and velocity at Mercury is also responsible for variations in the incoming plasma flux of roughly 1–2 orders of magnitude (Sarantos et al. 2007). Therefore, taking into account variations in both the IMF and the solar wind plasma flux, it is likely that the longitudinal accumulation of plasma driven by the 3:2 resonance would be hidden by such natural variability. The use of the effective shielding parameter α in Equation (2) remains, however, of deep interest, since it represents a first-order measure of a nonhomogeneous and time-varying process.

As recently highlighted by MESSENGER/FIPS observations of proton precipitation at the northern cusp (Raines et al. 2022), one pervasive characteristic of Mercury’s interaction with the solar wind is high variability. Our study, however, focuses on representative cases with fixed solar wind conditions; we then computed the effect of these fixed cases over two full Mercury orbits. In doing so, several types of events that may provide substantial contributions to space weathering (such as coronal mass ejections, CMEs; interplanetary shocks; and solar energetic particle, SEP, events) have been omitted. These extreme events profoundly alter the ability of the planetary magnetic field to shield the surface. From MESSENGER observations, Winslow et al. (2015) identified a total of 61 CMEs from 2011 March to 2014 September, corresponding to an occurring frequency of roughly one CME every 20 days. The increase in ram pressure associated with these events compresses the dayside magnetopause, increases the surface exposed to solar wind flux, and, in few abnormally strong and rare cases, completely rips off the dayside magnetosphere (Slavin et al. 2014, 2019; Winslow et al. 2017; Exner et al. 2018; Jia et al. 2019). Concerning SEP events, Gershman et al. (2015) inferred the high-latitude precipitation of solar energetic electrons onto the surface of Mercury for 11 SEP events. As SEP events include protons over 15 MeV and electrons up to 3 MeV in energy at substantial fluxes, they can make substantial contributions to space weathering over periods of hours to days (Lario et al. 2013). However, the details concerning the probability of all of these events occurring, as well as their full impact on space-weathering processes, remain poorly known at present.

Ion precipitation onto the surface of Mercury is one of the drivers of space weathering via ion sputtering and implantation. Space weathering alters the spectral properties of the regolith by darkening the surface, decreasing absorption band depths, and changing the spectral slope (reddening from the visible to near-infrared, blueing from the ultraviolet to the visible; Noble et al. 2007; Blewett et al. 2021). The infrared spectrometer MERTIS on board BepiColombo will be able to measure those spectral variations at Mercury (Maturilli et al. 2014; Hiesinger et al. 2020).

The geographical distributions of proton fluxes at the surface of Mercury shown in Figure 3 when compared to spectral surface properties can provide key information to infer the role of solar wind ion irradiation in the spectral processing of the surface. However, given the strong dependence of these maps on the time-variable IMF direction, we introduced the proton effective shielding parameter $\alpha_p \approx 20$ in Equation (2). The use of this parameter will enable researchers to compare the partially shielded surface of Mercury with the unshielded surfaces of the Moon and unmagnetized asteroids such as Ryugu (Sawada et al. 2017) and Bennu (Lauretta et al. 2017), paving the way to comparative space-weathering studies.

Space-weathering studies of the Hermean regolith rely on comparisons with the Moon and asteroids (Domingue et al. 2014). Understanding how the magnetic field of Mercury shields the planetary surface compared to that of other unmagnetized bodies is a key point to comparatively study the effects of space weathering on solar system bodies. At Mercury, in this work, we showed that the surface is exposed, on average, to $\sim 2 \times 10^{14}$ protons cm^{-2} integrating over two full Mercury orbits. At the Moon, using Equation (1) and considering a solar wind flux of 3×10^8 protons $\text{cm}^{-2} \text{s}^{-1}$, we find a fluence of $\sim 10^{15}$ protons cm^{-2} for the same time period (this value would be reduced to $\sim 7 \times 10^{14}$ protons cm^{-2} if considering zero proton flux when the Moon crosses Earth’s magnetosphere; Poppe et al. 2018). For main-belt asteroids, this fluence is further reduced by a factor of ~ 5 – 10 due to the increased distance from the Sun. Therefore, Mercury is bombarded by roughly three to five times fewer protons as compared to the Moon and roughly the same amount of protons as compared to a main-belt asteroid. At Mercury, the magnetic field screening compensates for the increase in solar wind flux as compared to the Moon. In this work, we neglected the interplay between ion irradiation and micrometeoroid processes such as impact gardening and comminution. Given that the micrometeoroid impactor flux at Mercury is about a factor of 40 higher than at the Moon (Pokorný et al. 2018, 2019; value obtained by comparing Figures 24 and 7 in these papers, respectively), this interplay might be important and should be addressed in future works.

Space weathering of Mercury’s surface has consequences for the remotely sensed properties of the regolith, namely, the determination of composition via color and spectral properties. Composition, the identification of both specific minerals and their abundances, is based on the detection and strength of absorption features. Space weathering by both solar wind irradiation and micrometeoroid impacts reduces the strength of absorption features. For example, the $1 \mu\text{m}$ band diagnostic of the mineral olivine can be completely masked by the formation of a small amount of nanophase iron ($\sim 1\%$ in weight of np-Fe^0) via solar wind irradiation and micrometeoroid impact-generated vapor (Kohout et al. 2014). At Mercury, the MESSENGER infrared spectrometer MASCS/VNIR (McClintock & Lankton 2007) showed no distinct spectral features throughout the visible to near-infrared except for the possible indication of sulfide mineralogy within the hollows (Vilas et al. 2016). Given the reduced proton fluence onto Mercury’s surface compared to the Moon (by roughly a factor of 3–5), we suggest that ion irradiation is not the main process at play in reducing spectral band signatures at Mercury.

4.2. Magnetosphere as an Accelerator and Decelerator: The Effect of a Magnetic Field on the Energy Distribution of Particles at the Surface

Our numerical simulations show that the energy distributions of both protons and electrons are affected differently by the Hermean magnetosphere. On the one hand, the protons impacting the surface are composed of one low-energy population (around ~ 200 eV) and one moderate-to-high-energy population (around ~ 1 keV). On the other hand, the electrons impacting the surface have a moderate energy of the order of ~ 0.1 – 1 keV. The fluences of these different populations at the surface are summarized in Table 1.

Our results on the proton energy distribution at the surface are key to reliably modeling the exosphere of Mercury. Solar wind protons contribute to the exosphere of Mercury via ion sputtering. Ion sputtering is usually included in exosphere models assuming a monochromatic energy of 1 keV amu^{-1} (e.g., Killen et al. 2022; Morrissey et al. 2022). This is a good approximation for protons in the solar wind, as shown by the orange curves in Figures 7(a) and (b). However, this is not a good approximation at the Hermean surface, where the proton distribution (in blue in Figures 7(a) and (b)) shows a large population at lower energies coming from the interaction with the bow shock. Protons below ~ 500 eV weakly contribute to ion sputtering (Eckstein 2007). Our modeling suggests that only $\sim 60\%$ of the total number of precipitating protons will have significant sputtering yields. From the fluences in Table 1, we see that this value changes with latitude. Around the poles, $\sim 50\%$ of the protons are efficient for sputtering (fluence of $\sim 1.7 \times 10^{14} \text{ protons cm}^{-2}$), whereas around the equator, this value goes to 100% with a fluence of $\sim 0.7 \times 10^{14} \text{ protons cm}^{-2}$. This mixture of spatial and energy dependence of the precipitating proton flux is a key ingredient that should be accounted for in the modeling of the Hermean magnetosphere and exosphere in the future.

Another major release mechanism for volatiles into Mercury's exosphere is photon-stimulated desorption (PSD; McGrath et al. 1986; Killen et al. 1990; Madey et al. 1998; Leblanc et al. 2022), a process that is enhanced by ion bombardment (McGrath et al. 1986; Mura et al. 2009; Leblanc et al. 2022). The coupling of these two processes is thought to produce a sodium exosphere in regions typical of ion sputtering but with the high efficiency and lower energy distribution of PSD. Estimates and patterns of volatile release via PSD will be modulated by the actual flux and energies of ions to the surface.

Solar wind electrons contribute to the exosphere of Mercury via ESD. This process is usually neglected in state-of-the-art exosphere models due to the lack of quantitative information on the flux and energy of precipitating electrons. Past works (McLain et al. 2011; Schriver et al. 2011) estimated that ESD can generate as many neutrals as ion sputtering at Mercury; however, such estimates come with large uncertainties. In our work, we provide quantitative estimates of the electron fluence and energy distribution at the surface of Mercury that will help to better evaluate the relevance of ESD as a source process for the exosphere of Mercury. The high-resolution maps in Figure 5 and the coarse grid values in Table 1, as well as the energy distribution in Figures 7(c) and (d), can be used to advance the exosphere modeling at Mercury including ESD.

Electrons accelerated within Mercury's magnetosphere in the range of 0.5 – 10 keV drive X-ray emissions from the surface via

XRF. While this process does not affect the chemistry of the surface, it allows the detection and mapping of regions of electron precipitation. Such emission has been observed by the XRS instrument on board MESSENGER for lines of Si $K\alpha$ (around 2 keV) and Ca $K\alpha$ (around 4 keV; Lindsay et al. 2016, 2022). This emission is driven by keV electrons accelerated in the magnetosphere by magnetic reconnection, as shown by Lavorenti et al. (2023) and discussed in Section 3.2. However, the XRS observations had a limited energy resolution, and the surface coverage was constrained by MESSENGER's orbit. The MIXS instrument on board BepiColombo (Bunce et al. 2020) will extend the XRS observations by providing (i) more coverage in the southern hemisphere of Mercury; (ii) a higher energy resolution, allowing the separation of the Mg, Al, and Si lines; (iii) a larger energy range, enabling the observations of lines from Na, Fe, and O; and (iv) an improved spatial resolution of $\lesssim 10$ km under optimal conditions that will allow better spatial characterization of regions of electron precipitation. The novel capabilities of MIXS to detect more and lower-energy fluorescence lines, coupled with electron observations from the Mio/MEA instrument (Saito et al. 2021), will help to constrain the energy spectrum and source process of precipitating \sim keV electrons at Mercury. The electron precipitation maps in Figure 5 coupled with surface composition models will help to interpret the future MIXS observations of electron-induced XRF at Mercury. From the maps in Figure 5, indirect information on the IMF direction can also be derived from the distribution of XRF onto the surface.

Surface charging at Mercury remains an open question at present. From the precipitating fluxes of protons and electrons computed in Section 3, we note a clear tendency of the surface to be negatively charged (the electron mean fluence is around a factor of 2 higher than that of protons, as shown in Table 1), at least on the nightside of the planet or within shadow in the dayside. This is somewhat expected given the higher mobility of electrons as compared to protons. Nonetheless, at this stage, it is hard to make any definitive conclusions about surface charging from our simulations given the lack of (i) sub-Debye-length kinetic physics in our implicit PIC code and (ii) photoelectron emission from the surface of Mercury in our model that is essential to constraining surface charging in illuminated regions of the Hermean surface. Future works could address this question using explicit PIC codes resolving the sub-Debye-length plasma–surface interactions, as well as including photoelectron emission from the illuminated surface. Proton and electron fluxes from the maps in this work (Figures 3)–(6)) could then be used as boundary conditions for such smaller-scale simulations.

5. Conclusion

From numerical simulations of the interaction of Mercury's magnetic field with solar wind plasma (protons and electrons), we have computed particle precipitation maps onto the planetary surface integrated over two full Mercury orbits (176 Earth days). Our results are as follows.

1. Mercury's 3:2 spin–orbit resonance has a weak effect on the time-integrated plasma precipitation pattern onto the surface. The surface pattern of precipitating plasma more strongly depends on the upstream magnetic field direction.

2. Mercury's weak magnetic field is able to shield, on average, 90% of the impinging solar wind protons and electrons.
3. Mercury's bow shock and magnetosphere tend to broaden the proton energy distribution going from the solar wind to the surface. A considerable number of protons at the surface have energies below 500 eV (mostly at high latitudes) and above 1.5 keV (mostly at low latitudes).
4. Mercury's magnetosphere tends to extend the electron energy distribution to high energies, with most of the electrons at the surface found in the range 0.1–10 keV.

Our results demonstrate the complexity of Mercury's geographical plasma precipitation and paves the way for future quantitative studies addressing the (i) space weathering of Mercury's regolith; (ii) plasma-driven source processes for Mercury's exosphere, such as ion sputtering and ESD; and (iii) electron-induced XRF emission from Mercury's regolith. The data used throughout the paper are publicly available at Lavorenti et al. (2023).

Acknowledgments

F.L. and P.H. acknowledges TGCC under allocations AP010412622 and A0100412428. F.L. acknowledges the CINECA award under the ISCRA initiative for the availability of high-performance computing resources and support. F.L. and P.H. acknowledge the support of CNES for the BepiColombo mission. F.L. acknowledges ESA support of the PhD. This research was supported by the ISSI in Bern (ISSI International Team project No. 525). J.R. was supported by NASA Discovery Data Analysis grant 80NSSC20K1148. S.A. is supported by JSPS KAKENHI No. 22J01606. D.D., E.A.J., and D.W.S. are supported by NASA Solar System Workings grant 80NSSC22K0099.

ORCID iDs

Federico Lavorenti  <https://orcid.org/0000-0002-2893-3588>
 Elizabeth A. Jensen  <https://orcid.org/0000-0003-0216-6621>
 Francesco Califano  <https://orcid.org/0000-0002-9626-4371>
 Deborah Domingue  <https://orcid.org/0000-0002-7594-4634>
 Simon Lindsay  <https://orcid.org/0000-0002-2655-2589>
 Daniel Wolf Savin  <https://orcid.org/0000-0002-1111-6610>

References

Anderson, B. J., Johnson, C. L., Korth, H., et al. 2012, *JGRE*, **117**, E00L12
 Bauch, K. E., Hiesinger, H., Greenhagen, B. T., & Helbert, J. 2021, *Icar*, **354**, 114083
 Belmont, G., Rezeau, L., Riconda, C., & Zaslavsky, A. 2019, in *Introduction to Plasma Physics*, ed. G. Belmont et al. (Amsterdam: Elsevier), 195
 Benkhoff, J., Murakami, G., Baumjohann, W., et al. 2021, *SSRv*, **217**, 90
 Benna, M., Anderson, B. J., Baker, D. N., et al. 2010, *Icar*, **209**, 3
 Blewett, D. T., Denevi, B. W., Cahill, J. T. S., & Klima, R. L. 2021, *Icar*, **364**, 114472
 Bunce, E. J., Martindale, A., Lindsay, S., et al. 2020, *SSRv*, **216**, 126
 David, L., Fraschetti, F., Giacalone, J., et al. 2022, *ApJ*, **928**, 66
 Dewey, R. M., Slavin, J. A., Raines, J. M., Azari, A. R., & Sun, W. 2020, *JGRA*, **125**, e28112
 DiBraccio, G. A., Slavin, J. A., Boardsen, S. A., et al. 2013, *JGRA*, **118**, 997
 Domingue, D. L., Chapman, C. R., Killen, R. M., et al. 2014, *SSRv*, **181**, 121
 Eckstein, W. 2007, *Sputtering Yields* (Berlin: Springer), 33
 Exner, W., Heyner, D., Liuzzo, L., et al. 2018, *P&SS*, **153**, 89
 Exner, W., Simon, S., Heyner, D., & Motschmann, U. 2020, *JGRA*, **125**, e2019JA027691
 Fatemi, S., Poppe, A. R., & Barabash, S. 2020, *JGRA*, **125**, e27706
 Gershman, D. J., Raines, J. M., Slavin, J. A., et al. 2015, *JGRA*, **120**, 8559

Gershman, D. J., Slavin, J. A., Raines, J. M., et al. 2013, *JGRA*, **118**, 7181
 Glass, A. N., Raines, J. M., Jia, X., et al. 2022, *JGRA*, **127**, e2022JA030969
 Haggerty, C. C., Shay, M. A., Drake, J. F., Phan, T. D., & McHugh, C. T. 2015, *GeoRL*, **42**, 9657
 Hiesinger, H., Helbert, J., Alemanno, G., et al. 2020, *SSRv*, **216**, 110
 James, M. K., Imber, S. M., Bunce, E. J., et al. 2017, *JGRA*, **122**, 7907
 Jia, X., Slavin, J. A., Poh, G., et al. 2019, *JGRA*, **124**, 229
 Kallio, E., & Janhunen, P. 2003, *AnGeo*, **21**, 2133
 Kidder, A., Winglee, R. M., & Harnett, E. M. 2008, *JGRA*, **113**, A09223
 Killen, R. M., Morrissey, L. S., Burger, M. H., et al. 2022, *PSJ*, **3**, 139
 Killen, R. M., Potter, A. E., & Morgan, T. H. 1990, *Icar*, **85**, 145
 Kohout, T., Čuda, J., Filip, J., et al. 2014, *Icar*, **237**, 75
 Korth, H., Anderson, B. J., Raines, J. M., et al. 2011, *GeoRL*, **38**, L22201
 Lario, D., Aran, A., Gómez-Herrero, R., et al. 2013, *ApJ*, **767**, 41
 Lauretta, D. S., Balram-Knutson, S. S., Beshore, E., et al. 2017, *SSRv*, **212**, 925
 Lavorenti, F., Henri, P., Califano, F., et al. 2022, *A&A*, **664**, A133
 Lavorenti, F., Henri, P., Califano, F., et al. 2023, *A&A*, **674**, A153
 Lavorenti, F., Jensen, E., Aizawa, S., et al. 2023, Maps of solar wind plasma precipitation onto Mercury's surface: a geographical perspective [Data set], Zenodo, doi:10.5281/zenodo.7927373
 Leblanc, F., Schmidt, C., Mangano, V., et al. 2022, *SSRv*, **218**, 2
 Lindsay, S. T., Bunce, E. J., Imber, S. M., et al. 2022, *JGRA*, **127**, e29675
 Lindsay, S. T., James, M. K., Bunce, E. J., et al. 2016, *P&SS*, **125**, 72
 Madey, T. E., Yakshinskiy, B. V., Ageev, V. N., & Johnson, R. E. 1998, *JGR*, **103**, 5873
 Mangano, V., Massetti, S., Milillo, A., et al. 2015, *P&SS*, **115**, 102
 Markidis, S., Lapenta, G., & Rizwan-uddin 2010, *Mathematics and Computers in Simulation*, **80**, 1509
 Massetti, S., Orsini, S., Milillo, A., et al. 2003, *Icar*, **166**, 229
 Massetti, S., Orsini, S., Milillo, A., & Mura, A. 2007, *P&SS*, **55**, 1557
 Maturilli, A., Helbert, J., John, J. M., St. et al. 2014, *E&PSL*, **398**, 58
 McClintock, W. E., & Lankton, M. R. 2007, *SSRv*, **131**, 481
 McGrath, M. A., Johnson, R. E., & Lanzerotti, L. J. 1986, *Natur*, **323**, 694
 McLain, J. L., Sprague, A. L., Grieves, G. A., et al. 2011, *JGRE*, **116**, E03007
 Meyer-Vernet, N. 2007, *Basics of the Solar Wind* (Cambridge: Cambridge Univ. Press)
 Morrissey, L. S., Tucker, O. J., Killen, R. M., Nakhla, S., & Savin, D. W. 2022, *ApJL*, **925**, L6
 Mura, A., Orsini, S., Milillo, A., et al. 2005, *Icar*, **175**, 305
 Mura, A., Wurz, P., Lichtenegger, H. I. M., et al. 2009, *Icar*, **200**, 1
 Noble, S. K., Pieters, C. M., & Keller, L. P. 2007, *Icar*, **192**, 629
 Ogilvie, K. W., Scudder, J. D., Hartle, R. E., et al. 1974, *Sci*, **185**, 145
 Phan, T. D., Drake, J. F., Shay, M. A., et al. 2014, *GeoRL*, **41**, 7002
 Poh, G., Slavin, J. A., Jia, X., et al. 2017, *GeoRL*, **44**, 678
 Pokorný, P., Janches, D., Sarantos, M., et al. 2019, *JGRE*, **124**, 752
 Pokorný, P., Sarantos, M., & Janches, D. 2018, *ApJ*, **863**, 31
 Poppe, A. R., Farrell, W. M., & Halekas, J. S. 2018, *JGRE*, **123**, 37
 Raines, J. M., Dewey, R. M., Staudacher, N. M., et al. 2022, *JGRA*, **127**, e2022JA030397
 Saito, Y., Delcourt, D., Hirahara, M., et al. 2021, *SSRv*, **217**, 70
 Sarantos, M., Killen, R. M., & Kim, D. 2007, *P&SS*, **55**, 1584
 Sawada, H., Okazaki, R., Tachibana, S., et al. 2017, *SSRv*, **208**, 81
 Schriver, D., Trávníček, P., Ashour-Abdalla, M., et al. 2011, *P&SS*, **59**, 2026
 Schriver, D., Trávníček, P. M., Anderson, B. J., et al. 2011, *GeoRL*, **38**, L23103
 Schwartz, S. J., Goodrich, K. A., Wilson, L. B., et al. 2022, *JGRA*, **127**, e2022JA030637
 Shay, M. A., Haggerty, C. C., Phan, T. D., et al. 2014, *PhPI*, **21**, 122902
 Slavin, J. A. 2004, *AdSpR*, **33**, 1859
 Slavin, J. A., DiBraccio, G. A., Gershman, D. J., et al. 2014, *JGRA*, **119**, 8087
 Slavin, J. A., Krimigis, S. M., Acuña, M. H., et al. 2007, *SSRv*, **131**, 133
 Slavin, J. A., Middleton, H. R., Raines, J. M., et al. 2019, *JGRA*, **124**, 6613
 Solomon, S. C., McNutt, R. L., Gold, R. E., & Domingue, D. L. 2007, *SSRv*, **131**, 3
 Sun, W. J., Raines, J. M., Fu, S. Y., et al. 2017, *GeoRL*, **44**, 8149
 Tóth, G., Chen, Y., Gombosi, T. I., et al. 2017, *JGRA*, **122**, 10,336
 Trávníček, P., Hellinger, P., & Schriver, D. 2007, *GeoRL*, **34**, L05104
 Trávníček, P. M., Hellinger, P., Schriver, D., et al. 2009, *GeoRL*, **36**, L07104
 Trávníček, P. M., Schriver, D., Hellinger, P., et al. 2010, *Icar*, **209**, 11
 Vilas, F., Domingue, D. L., Helbert, J., et al. 2016, *GeoRL*, **43**, 1450
 Winslow, R. M., Anderson, B. J., Johnson, C. L., et al. 2013, *JGRA*, **118**, 2213
 Winslow, R. M., Lugaz, N., Philpott, L. C., et al. 2015, *JGRA*, **120**, 6101
 Winslow, R. M., Philpott, L., Paty, C. S., et al. 2017, *JGRA*, **122**, 4960
 Wurz, P., Fatemi, S., Galli, A., et al. 2022, *SSRv*, **218**, 10